## SPACE SCIENCES

# Direct observations of cross-scale wave-particle energy transfer in space plasmas

Jing-Huan Li[1,2,3], Xu-Zhi Zhou[1]*, Zhi-Yang Liu[4], Shan Wang[1], Yoshiharu Omura[2,5], Li Li[1], Chao Yue[1], Qiu-Gang Zong[1,2], Guan Le[6], Christopher T. Russell[7], James L. Burch[8]

The collisionless plasmas in space and astrophysical environments are intrinsically multiscale in nature, behaving as conducting fluids at macroscales and kinetically at microscales comparable to ion and/or electron gyroradii. A fundamental question in understanding the plasma dynamics is how energy is transported and dissipated across scales. Here, we present spacecraft measurements in the terrestrial foreshock, a region upstream of the bow shock where the solar wind population coexists with the reflected ions. In this region, the fluid-scale, ultralow-frequency waves resonate with the reflected ions to modify the velocity distributions, which in turn cause the growth of the ion-scale, magnetosonic-whistler waves. The latter waves then resonate with the electrons, and the accelerated electrons contribute to the excitation of electron-scale, high-frequency whistler waves. These observations demonstrate that the chain of wave-particle resonances is an efficient mechanism for cross-scale energy transfer, which could redistribute the kinetic energy and accelerate the particles upstream of the shocks.

## INTRODUCTION

In the plasma universe, the energy and momentum exchange usually cannot be supported by collisions as in ordinary gases but rather rely on the variety of electromagnetic and electrostatic waves. The coexistence of many different wave modes, together with the diverse particle species and energies, constitutes a highly coupled system where cross-scale processes occur via turbulent cascades, coherent wave-wave interactions, and/or resonant wave-particle interactions. The turbulent cascade or, equivalently, the nonlinear energy cascade toward finer scales in turbulent plasma is usually attributed to randomly phased electromagnetic perturbations mediating the cross-scale energy transfer (1–5). Nonlinear interactions could also take place between coherent waves, during which the wave energy is channeled toward higher frequencies (6, 7). Moreover, coherent wave-particle interactions could modulate particle distributions so that they become unstable to plasma waves at higher frequencies (8–14). These waves could eventually be absorbed through interactions with other particles.

The above processes, thought to be universal, are usually difficult to observe. A unique natural laboratory enabling in situ investigation of such processes is the near-Earth space, especially in recent years when high-resolution particle and field measurements are available via spaceborne instruments. A region of particular interest is Earth's foreshock, the upstream region of the terrestrial bow shock, where particles backstreaming from the bow shock interact with the background solar wind to accommodate a zoo of plasma waves (15, 16). One of the frequently observed waves is the fast/magnetosonic mode waves, typically in the ultralow-frequency (ULF; from 1 mHz to 10 Hz) range after being Doppler-shifted into the spacecraft rest frame (15). These waves are excited by the backstreaming ions via electromagnetic ion/ion resonant

or nonresonant instabilities (17). The nonlinear steepening of the ULF waves leads to the formation of sharp magnetic bumps known as "shocklets" (18, 19), typically accompanied by magnetosonic-whistler wave packets (sometimes referred to as ion-scale fast-magnetosonic waves or low-frequency fast-magnetosonic waves) radiating sunward in the plasma rest frame (15, 20, 21). Similar signatures have been also reported near interplanetary shocks (22) and other planetary (23–26) or cometary environments (27, 28). Moreover, the magnetosonic-whistler wave packets can modulate whistler waves at higher frequencies (13, 14). The complex variety of waves play a critical role in the energy exchange with solar wind particles (13, 14, 29–33), although the detailed processes responsible for energy dissipation at kinetic scales remain unclear due to the lack of direct observations.

Here, we present in situ observations from Magnetospheric Multiscale (MMS) spacecraft of large-amplitude electromagnetic waves in Earth's foreshock, providing direct evidence for cross-scale energy transfer via coherent wave-particle interactions. The observations show that the reflected ions provide the free energy to excite the ULF waves. As the ULF waves grow, the ions undergo simultaneous resonance with large-amplitude ULF and magnetosonic-whistler waves. The former resonance produces a new population on top of the background solar wind, leading to the magnetosonic-whistler wave growth and consequently the energy transfer from fluid to ion scales. The energy is then transferred, via a resonance process, to the electron population, which in turn contributes to the excitation of electron-scale whistler waves at higher frequencies. In other words, we identify observationally the entire chain of wave-particle energy flow from fluid- to ion- and eventually to electron scales. The results also indicate that anomalous resonance, a nonlinear resonance occurring when the wave amplitude is large enough to modify the classical resonance condition (34), plays an important role in the cross-scale energy transfer processes.

[1]School of Earth and Space Sciences, Peking University, Beijing, China. [2]State Key Laboratory of Lunar and Planetary Sciences, Macau University of Science and Technology, Macau, China. [3]Swedish Institute of Space Physics, Uppsala, Sweden. [4]Institut de Recherche en Astrophysique et Planetologie, CNES-CNRS, Universite Toulouse III, Paul Sabatier, Toulouse, France. [5]Research Institute for Sustainable Humanosphere, Kyoto University, Kyoto, Japan. [6]NASA Goddard Space Flight Center, Greenbelt, MD, USA. [7]Institute of Geophysics and Planetary Physics, University of California, Los Angeles, CA, USA. [8]Southwest Research Institute, San Antonio, TX, USA.
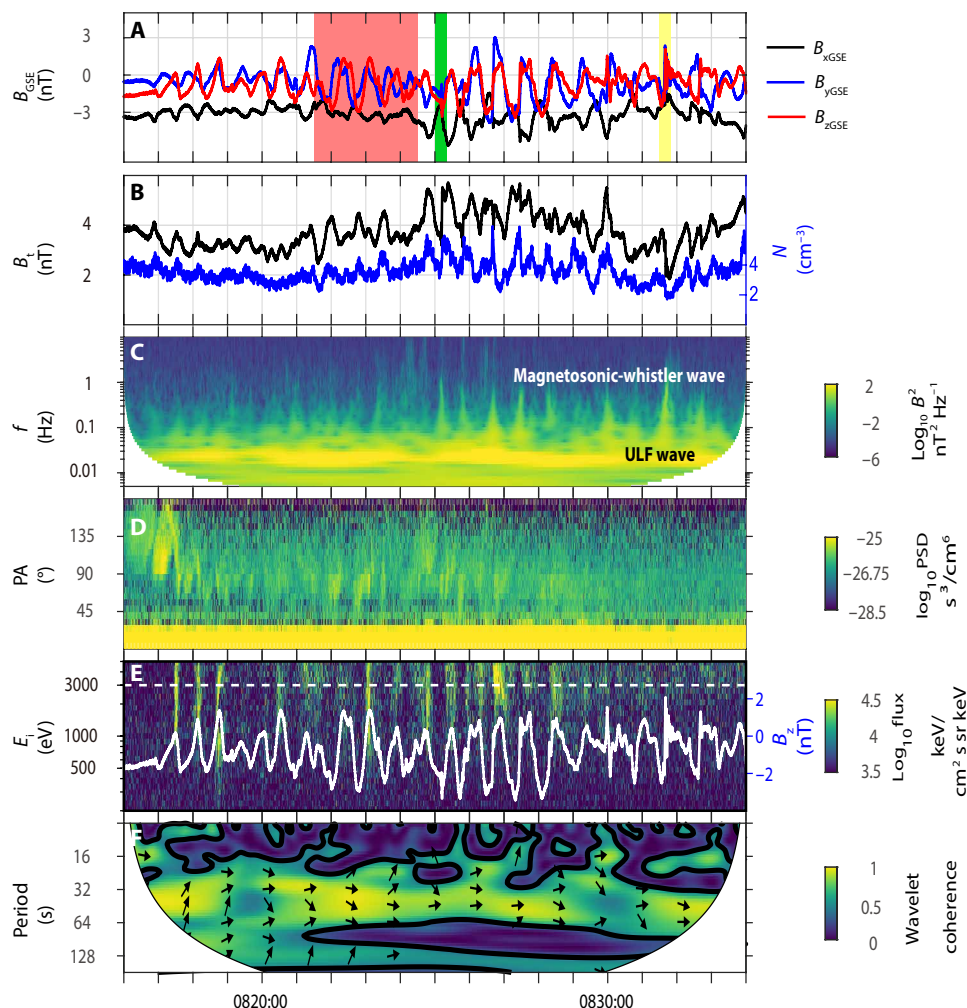
*Corresponding author. Email: xzzhou@pku.edu.cn

## RESULTS

### Event #1: Overview

The event occurred on 7 January 2021 when the four-spacecraft MMS constellation stayed in the foreshock, at [23.7, 15.4, 0.3] Earth Radius (Re) in the Geocentric Solar Eclipse (GSE) coordinates (with $x$ axis pointing sunward and $z$ axis perpendicular to the ecliptic

plane). The MMS data used include electric field measurements from electric field double probes, magnetic field measurements from a flux-gate magnetometer, and ion/electron velocity distributions from fast plasma investigation (FPI) at lower energies and fly's eyes energetic particle spectrometer (FEEPS) at higher energies. These high-resolution observations offer a rare opportunity to study the wave-particle interactions quantitatively (35–37).

Figure 1 presents an 18-min overview of the MMS1 observations, in which the magnetic field components in GSE (Fig. 1A) show strong oscillations (mostly in the $yz$ plane) with a period of ~45 s. The ULF oscillations of the field strength (Fig. 1B, black line) are nearly in phase with the oscillations of the electron number density (or plasma density, see blue line in Fig. 1B), which is an important feature of fast/magnetosonic waves commonly observed in the foreshock (38, 39). The background magnetic field, computed via a long-term average of the field, is almost always antisunward (or, equivalently, along the solar wind flow direction), with a magnitude of ~3 nT comparable to the wave amplitude.

To facilitate the analysis of ULF wave-particle interactions, we setup a background field-aligned coordinate (FAC) system, in which the parallel direction $e_\parallel$ is along the background field in the GSE $-x$ direction. Therefore, the FAC system is well aligned with GSE, with the $e_{\perp 1}$ and $e_{\perp 2}$ axes along $-z$ and $-y$ directions, respectively. In the FAC system, we accordingly define the pitch angle of any given particle as the angle between its velocity and $e_\parallel$ and its gyro-phase angle as the angle between its perpendicular velocity and the $e_{\perp 1}$ direction.

Figure 1C shows the wavelet power spectrum of the transverse magnetic perturbations (the $B_y$ and $B_z$ components), in which the persistence of large-amplitude ULF waves is manifested by an enhanced power near 0.02 Hz. The wavelet spectrum also shows intermittent enhancements of the wave power at frequencies above 0.1 Hz. These high-frequency wave packets are magnetosonic-whistler precursors (15) associated with the nonlinear steepening of the ULF waves (19). The detailed wave properties are determined below.

**Fig. 1. MMS observations of ULF waves, ion distributions, and magnetosonic-whistler waves.** (**A**) Magnetic field in the GSE coordinates. (**B**) Magnetic field strength, with the plasma number density superimposed. (**C**) Wavelet power spectral density of the perpendicular magnetic field. (**D**) Pitch angle spectra of ions within the energy range between 1.5 and 4.5 keV. (**E**) Energy spectrum for the ions along the $-z$ direction in the GSE coordinates, with $B_z$ component of magnetic field superimposed. (**F**) Wavelet coherence between the flux of the 3-keV ions moving in the $-z$ direction and magnetic field $B_z$ component. The arrows represent their phase differences, with rightward arrows indicating the in-phase relationship. PA, pitch angle.

### Event #1: Wave properties

We first focus on the red-shadowed interval in Fig. 1 (between 0821:30 and 0824:30 UT). The ULF wave field in the $yz$ plane denotes a left-hand polarization, since the quasi-sinusoidal $B_y$ variations always lead $B_z$ in phase by $\sim\pi/2$. After that, the ULF waves become linearly polarized (see Fig. 1A, after 0825:00). According to (*19*), the polarization change of the ULF waves is likely caused by the dispersive propagation (*40*) of the newly generated, high-frequency wave packets, which spread in space to modify the ULF wave properties.

We next estimate the phase speed of the ULF waves via a singular value decomposition (SVD) analysis of the electromagnetic fields (see fig. S1 for details) (*41*). The ULF waves, with frequency $\omega_{ULF} \sim 0.14$ rad/s, propagate quasi-parallel to the bulk flow direction at the velocity of $v_{ULF} = 433$ km/s. This speed is slightly lower than the plasma bulk velocity $v_b$ (465 km/s along $-x$), implying that the left-hand polarized ULF waves in the spacecraft frame are intrinsically right-hand polarized, sunward-propagating waves in the plasma frame (*15*, *42*). The small parallel wave number, $k_{ULF} \sim 0.04/r_i$ ($r_i = 121$ km is the ion inertial length, over which the ions are decoupled from the magnetic field), indicates that they are fluid-scale waves.

The properties of high-frequency wave packets are also analyzed. One of the most prominent wave packets occurred between 0831:30 and 0831:50 UT (the yellow-shadowed interval in Fig. 1, with zoom-in views shown in the right column of fig. S2), which exhibits a left-hand polarization and a decreasing wave period. Note that a revised FAC system must be adopted, since the fluid-scale ULF waves contribute to the background field of the high-frequency waves. The revised FAC is established by defining $\mathbf{e}_\parallel$ via a 10-s running averaged field $\mathbf{B}_0$, $\mathbf{e}_{\perp 2}$ as the cross-product of $z$ and $\mathbf{e}_\parallel$, and $\mathbf{e}_{\perp 1}$ completing the triad. We then determine, based on SVD analysis (fig. S3), the phase speed ($v_{mw} = 378$ km/s along $-x$) of the high-frequency waves to be lower than the bulk velocity $v_b$. The reversed wave propagation (sunward in the plasma frame) indicates an intrinsic right-hand polarization after considering the Doppler effect, which supports the identification of magnetosonic-whistler waves (*20*). The observed frequency dispersion originates from the larger phase speed of the waves at higher than at lower frequencies (*40*). The parallel wave number, $k_{mw} \sim 0.91/r_i$ at the typical frequency $\omega_{mw} = 2.83$ rad/s, indicates that they are ion-scale waves.

In this event, there are other packets of high-frequency waves with different properties. One of the examples occur between 0825:00 and 0825:20 UT (the green-shadowed interval in Fig. 1), with zoom-in views presented in the left column of fig. S2. This packet exhibits a right-hand polarization and an increasing wave period in the spacecraft frame, apparently reversed from the wave packet discussed earlier (compare the left and right panels in fig. S2). The apparent reversal originates from the higher wave phase speed (estimated to be ~640 km/s in the spacecraft frame) than the solar wind speed in the $-x$ direction. Therefore, unlike the wave packet discussed earlier, the wave polarization and dispersion properties remain unchanged in the plasma rest frame, which also supports the identification of magnetosonic-whistler waves.
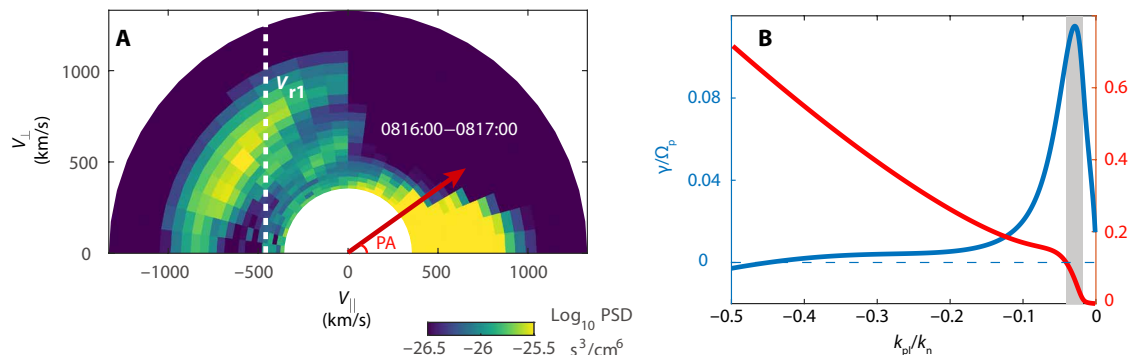
### Event #1: ULF wave interaction with the ions

Figure 1 (D to F) shows the ion distributions and their correlations with the ULF waves. Figure 1D displays the ion pitch angle spectra within the 1.5- to 4.5-keV energy range, in which the high phase-space densities (PSDs) in the parallel direction (pitch angle ~0°) correspond to the intense solar wind flow. During the first 2 min, there is another population near the pitch angle of ~135°, which are beams reflected from the terrestrial bow shock. The reflected population, mainly composed of protons, can be also seen in Fig. 2A, the averaged ion distributions in the $v_\parallel$-$v_\perp$ plane from 0816:00 to 0817:00. The reflected protons in the foreshock have long been associated with ULF wave excitation through the ion/ion resonant instability (*17*, *42*), which can be examined by considering the classical cyclotron resonance condition below.

The parallel speed of a cyclotron-resonant particle, often called the resonance velocity, equals (in the nonrelativistic limit)

$$V_r = \frac{\omega \pm \Omega}{k_\parallel} \tag{1}$$

where $\omega$ is the wave angular frequency, $\Omega$ is the particle gyrofrequency, and $k_\parallel \neq 0$ is the parallel wave number. The resonance condition (Eq. 1) ensures that the wave frequency observed by the particle, after considering the Doppler shift to the particle's guiding center frame, matches its gyrofrequency so that a sustained wave-particle energy exchange could occur (*43*, *44*). Here, the + and − signs in Eq. 1 correspond to the situations in which the wave

**Fig. 2. The observed ion velocity distributions in the $v_\parallel - v_\perp$ plane and corresponding linear instability analysis.** (**A**) Ion velocity distributions in the spacecraft frame averaged from 0816:00 to 0817:00. The horizontal and vertical axes represent the parallel velocity $v_\parallel$ and the perpendicular velocity $v_\perp$, respectively, both defined in FAC coordinates. The angle from the horizontal ($v_\parallel$) axis represents the pitch angle (PA). The white dashed line delineates the proton cyclotron resonance velocity $V_{r1}$ for ULF waves. (**B**) Wave growth rate $\gamma$ (blue line, normalized by proton gyrofrequency $\Omega_p$) and dispersion relation $\omega_{pl}$ (red line, normalized by proton gyrofrequency $\Omega_p$) in plasma frame. The observed ULF wave numbers are located in the shadowed area, normalized by the ion inertial length $r_i = 1/k_n$.

polarization in the reference frame of interest has the opposite and the same handedness as the particle gyration, respectively (named anomalous and normal cyclotron resonances, respectively, see Materials and Methods and the Supplementary Materials for detailed explanations). In this event, the minus sign applies for resonant ions since the ULF waves are left-hand polarized in the spacecraft rest frame. Moreover, the observed ULF wave frequency $\omega_{ULF}$ is smaller than the proton gyrofrequency $\Omega_p$ (~0.29 rad/s), which indicates a negative $V_r$ (−458 km/s; see the dashed line in Fig. 2A) in the spacecraft frame. For a resonant proton at 3 keV, the pitch angle is 130°, which belongs to the reflected population.

On the basis of the observed particle distributions (Fig. 2A), we use a dispersion relation solver (see Materials and Methods for detailed parameters) (45) to confirm the linear excitation of fast/magnetosonic waves. Figure 2B shows the resultant dispersion relation (red line) and growth rate (blue line) of the waves, in which the sunward wave propagation is manifested by negative $k_{pl}$, the parallel wave number in the plasma frame. The wave number determined from observations (the shadowed region) corresponds to a positive wave growth rate ($\gamma > 0$), which indicates the excitation of fluid-scale ULF waves via cyclotron resonance (39, 46). The detailed wave properties and resonant conditions are given in table S1, with an illustration of wave dispersion relation and resonance conditions shown in fig. S4.

As the ULF waves grow, the reflected beams gradually disappear. However, there emerges another population in the pitch angle range from 40° to 90° (Fig. 1D), which is still separated from the solar wind flow near 0°. Also shown in Fig. 1D are periodic variations of ion PSDs within the 1.5- to 4.5-keV range, at approximately the ULF wave frequency. The wave-particle correlation can be better visualized in Fig. 1E, which displays the energy spectrum of the ions moving in the −z direction (pitch angle, ~90°) superimposed by the $B_z$ field (white line). Obviously, the periodic ion flux enhancements are one to one correlated with the $B_z$ peaks. Figure 1F shows the wavelet coherence (47) between the 3-keV ion flux and $B_z$ to delineate their correlation in the time-frequency domain, with the arrows representing the phase differences. The high coherence at the wave period of ~45 s, together with their in-phase relationship indicated by the horizontal arrows, demonstrates the phase-bunched ion distributions characterizing the occurrence of wave-particle resonance (42). On the basis of previous studies (29, 34, 48, 49), the phase-bunched feature can be also manifested as periodic, inclined stripes in the gyro-phase spectra if the waves are circularly polarized. Therefore, we select the red-shadowed interval in Fig. 1 (during which the waves are left-hand and nearly circularly polarized; see the ULF wave field $\mathbf{B}_{1,ULF}$ in Fig. 3A) to further analyze the ion distributions.

Figure 3 (B to D) shows the gyro-phase spectra for 3-keV ions (averaged over the four MMS spacecraft observations to improve the statistical significance) at the pitch angles of 40°, 90°, and 130°, respectively. In Fig. 3 (B and C), inclined stripes with enhanced PSDs in antiphase with $\mathbf{B}_{1,ULF}$ (see the white lines for the phase of $-\mathbf{B}_{1,ULF}$, defined by its angular difference from $\mathbf{e}_{\perp 1}$) appear periodically. This is a characteristic feature for wave-particle resonance, which can only be expected within finite energy and pitch angle ranges where the ions are locked in phase with the waves during their gyromotion (48). As discussed before, the classical picture of cyclotron resonance indicates the resonance velocity of $V_r = -458$ km/s, which corresponds to the pitch angle of 130° for 3-keV protons. This expectation contradicts to the phase-bunched signatures at pitch

angles of 40° to 90° (Fig. 3, B and C) but not 130° (Fig. 3D). Even if we consider a wide frequency range (0.12 to 0.18 rad/s) of the waves, the corresponding $V_r$ would vary between −600 and −300 km/s, still deviating markedly from the observations. Therefore, the classical theory of cyclotron resonance may not be appropriate during this interval with large wave amplitude.

To understand the apparent discrepancy, we invoke the scenario of anomalous resonance (34) (not to be confused with anomalous cyclotron resonance; see their definitions in Materials and Methods) for waves with large amplitude comparable to the background field $B_0$ ($B_{1,ULF}/B_0 \sim 2/3$ in this event). In this case, the particle angular velocity is not determined solely by the background $B_0$ but also modified by the wave electromagnetic field. Consequently, the resonance condition is nonlinearly revised (50) to ensure the match between the particle's modified angular frequency and the Doppler-shifted wave frequency. This scenario indicates that resonant particles could be phase-trapped within one of the two resonance islands centered at separated phase-space locations (51, 52), in phase and in antiphase with the wave magnetic field, respectively. The full resonance velocity is expressed by
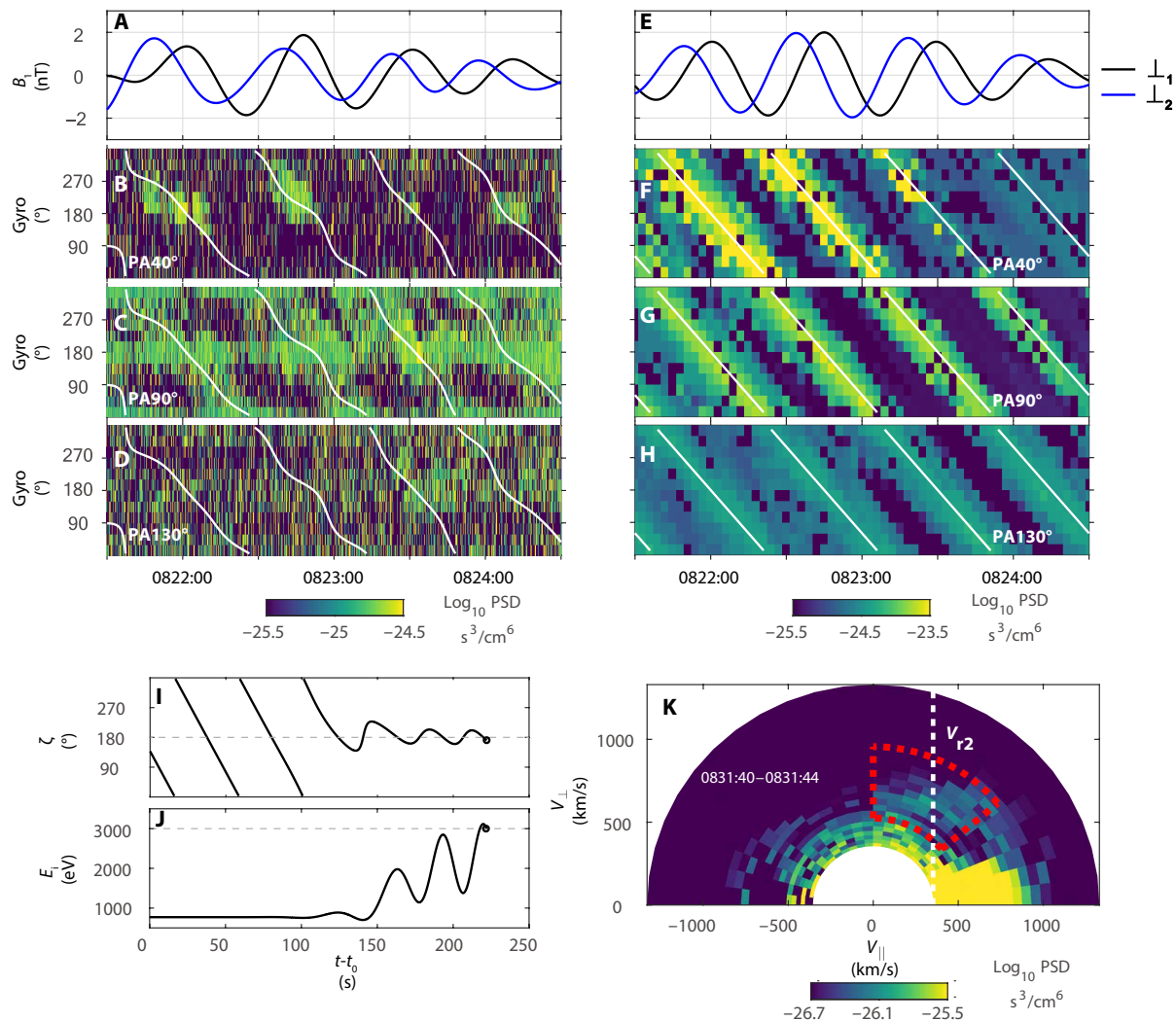
$$V_r' = \frac{(\omega - \Omega)v_\perp \mp \Omega_1 v_w}{k_\parallel v_\perp \mp \Omega_1} = V_r + \frac{V_r - v_w}{-1 \pm \frac{k_\parallel v_\perp}{\Omega_1}} \tag{2}$$

where the upper and lower signs correspond to the in-phase and in-antiphase resonance islands, respectively, $v_w$ represents the wave phase speed, $\Omega_1 = B_1 q / m$ is the nominal gyrofrequency associated with the wave field $B_1$, and $V_r$ is the classical cyclotron resonance velocity given by Eq. 1 (in which the minus sign applies). Note that Eq. 2 degenerates to the classical resonance condition (1) when the following criterion is satisfied (34)

$$\sqrt{\frac{B_1}{B_0}} \ll \sqrt{\frac{v_\perp^3}{|v_w - V_r|^3}} \tag{3}$$

Given a typical proton (3 keV, 45° pitch angle) in this event, the left and right sides are 0.82 and 0.47, respectively. Therefore, criterion (3) is not satisfied due to the large $B_1/B_0$ ratio, which explains the discrepancy between the observations and the expectations from cyclotron resonance. Since the ions in Fig. 3 (B to D) are phase-bunched in antiphase with the wave magnetic field, the lower sign in Eq. 2 applies in the calculation of anomalous resonance velocity, $V_r' = -67$ km s$^{-1}$ for the 3-keV ions. The velocity corresponds to the resonant pitch angle of 95° (rather than 130° based on Eq. 1). This is consistent with the observations of prominent phase-bunched signatures at 90° pitch angle for the 3-keV ions. At lower pitch angles (Fig. 3B), the resonant trapping is also made possible by the finite width of the resonance island. This scenario is further verified via test particle simulations.

The simulation, on the basis of the Liouville's theorem of PSD conservation along particle trajectories (53–55), follows a similar procedure as in (34). After constructing the initial ion distributions through the averaged measurements during the quiet period from 0816:00 to 0817:00, we launch a Gaussian-profiled wave packet propagating along the homogeneous background field and trace a series of test protons from an immobile virtual spacecraft backward in time for their initial velocities. The corresponding PSDs are thus determined via the Liouville's theorem. The detailed simulation setup and parameters are given in Materials and Methods. Figure 3 (E

**Fig. 3. MMS observations and simulation results of the ion distributions.** (**A**) The filtered ULF wave magnetic field $\mathbf{B}_{1,\text{ULF}}$ in FAC during the red-shadowed interval. (**B** to **D**) Gyro-phase spectra for 3-keV ions, at the pitch angles (PAs) of 40°, 90°, and 130°, respectively. The phase of $-\mathbf{B}_{1,\text{ULF}}$ is indicated by the white lines. (**E** to **H**) Simulation results in the same format as the observations in (A) to (D). (**I** and **J**) Temporal variations of $\zeta$ and kinetic energy $E_i$ for the typical proton. (**K**) The averaged ion distribution in the $v_\parallel - v_\perp$ plane from 0831:40 to 0831:44 in the spacecraft frame, with the white dashed line delineating the proton cyclotron resonance velocity $V_{r2}$ for magnetosonic-whistler waves. The area surrounded by the red box represents the phase-bunched ions in resonance with the ULF waves.

to H) shows the virtual observations of the ULF waves and the ion gyro-phase spectra at the pitch angles of 40°, 90°, and 130°, respectively. They display periodic, inclined stripes with enhanced PSDs in antiphase with the wave field $\mathbf{B}_{1,\text{ULF}}$, with stronger PSD variations at 40° and 90° than at 130°, a similar feature to the actual observations in Fig. 3 (A to D). We also analyze the typical ion trajectory (Fig. 3, I and J) to identify the trapping motion around the resonance island centered at $\zeta = 180°$ (see Fig. 3I, where $\zeta$ is the phase difference between $v_\perp$ and $B_1$), during which the particle's energy can be substantially increased (Fig. 3J). It is the acceleration that causes the periodic PSD enhancement in antiphase with the wave field, which is also consistent with the observations of enhanced PSDs in the pitch angle range between 40° and 90° (Fig. 1D). The consistency between observations and simulation results indicates efficient ion acceleration via anomalous resonance when the waves become strong enough (especially after 0818:00).

## Event #1: Magnetosonic-whistler wave interaction with the ions

We next study the interaction between the ions and the magnetosonic-whistler wave packets. Taking the yellow-shadowed interval (0831:30 to 0831:50) in Fig. 1 as an example, the magnetosonic-whistler wave properties determined above enable us to examine criterion (3) for the applicability of the classical cyclotron resonance. Here, the cyclotron resonance velocity, $V_r \sim 352$ km/s in the spacecraft frame, is close to the wave phase velocity $v_{wh} \sim 378$ km/s along the parallel direction, which indicates the satisfaction of criterion (3) and the applicability of the classical cyclotron resonance. The ions resonating with the magnetosonic-whistler waves overlap with those experiencing anomalous resonance with the ULF waves. Figure 3K shows the averaged ion distributions during this interval (within the $v_\parallel - v_\perp$ plane), in which the area surrounded by the box (energy range: 1.5 to 4.5 keV; pitch angle range: 40° to 90°) represents the

ions in anomalous resonance with the ULF waves. The ion PSDs within this area are higher than those in adjacent phase-space regions to form unstable distributions, which probably result from the sustained ion acceleration from the ULF waves. The white line, on the other hand, delineates the resonance velocity with the magnetosonic-whistler waves (see table S2 for wave properties and the associated resonance velocity). Since these ions could resonate simultaneously with the ULF and the magnetosonic-whistler waves, we speculate that the unstable ion distributions driven by the ULF waves could lead to the growth of the magnetosonic-whistler waves.

To validate this hypothesis, we calculate the energy transfer rate $\mathbf{J}_i \cdot \mathbf{E}_1$ between the ions and the magnetosonic-whistler waves (see Fig. 4) (9, 48, 56). Here, the ion current density $\mathbf{J}_i$ in the plasma rest frame represents the contribution from resonant ions within the box in Fig. 3K, and a Lorentz transformation is performed to ensure that the wave electric field $\mathbf{E}_1$ is also in the plasma frame. Figure 4B shows the 4-s running averaged energy transfer rate, which is predominantly negative to indicate the energy transfer from resonant ions to whistler waves. The transfer rate peaks at ~0.02 pW m$^{-3}$, suggesting that it may take 1.5 gyro periods for the magnetosonic-whistler waves to reach the amplitude of $B_1 = 1.5$ nT, close to previous simulation results (19). We also apply the dispersion relation solver based on the updated ion distributions (with detailed parameters given in Materials and Methods), to confirm that the linear wave growth rate, given in Fig. 4C, remains positive in the wave number range of interest ($k_{pl} \sim 1/r_i$). Therefore, the chain of wave-particle resonances provides an efficient way for energy transfer from fluid to ion scales.

### Event #1: Magnetosonic-whistler wave interaction with electrons
Figure 5 (A to E) shows the observed magnetosonic-whistler wave field $\mathbf{B}_{1,mw}$ and the electron gyro-phase spectra (averaged over MMS1, MMS2, and MMS3 observations, since MMS4 data are unavailable), in which the PSDs of electrons with pitch angles of 40° (Fig. 5, B and C) and 140° (Fig. 5, D and E) display periodic, inclined stripes in phase and in antiphase with $\mathbf{B}_{1,mw}$ (see the white lines for the phase of $-\mathbf{B}_{1,mw}$), respectively. These features indicate the coexistence of two resonance islands in phase and in antiphase with $\mathbf{B}_{1,mw}$, a manifestation of wave-particle anomalous resonance (34). The electron pitch angles satisfying the resonance condition are ~40° and ~140°, for the islands centered at $\zeta = 0°$ and 180°,
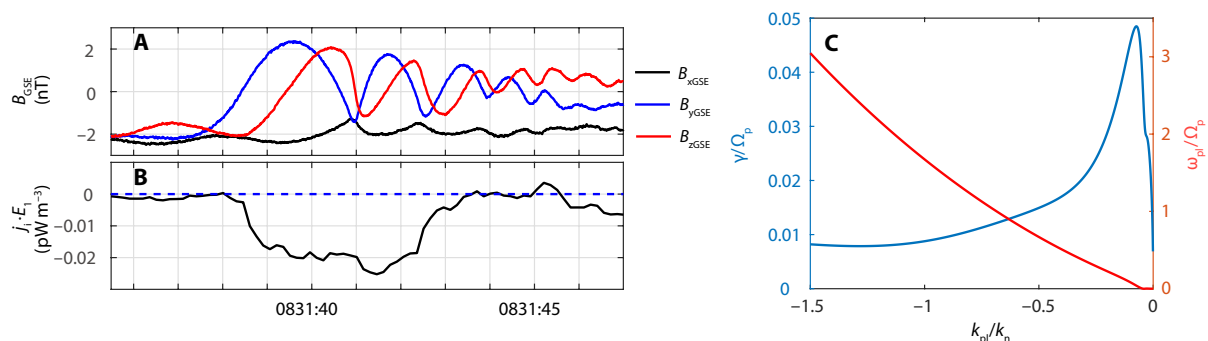
respectively. They agree with the observations in Fig. 5 (B to E). One may also determine the classical cyclotron resonance velocity through Eq. 1 (with the plus sign), to be $V_r = 4.7 * 10^4$ km/s, which corresponds to the parallel energy of ~7 keV. This energy is much larger than those in Fig. 5 (B to E) (17 to 67 eV), which is consistent with the fact that criterion (3) of classical cyclotron resonance is unsatisfied.

To validate the occurrence of anomalous resonance, test particle simulations following similar procedures are performed for the electrons, with wave parameters and initial electron distributions given in Materials and Methods. The simulation results in Fig. 5 (F to J) reproduce the signatures of electrons concentrated in-phase and in-antiphase with the wave magnetic field. The typical electron trajectories (fig. S5) also show the trapping of resonant electrons, during which they can be accelerated by the magnetosonic-whistler waves.
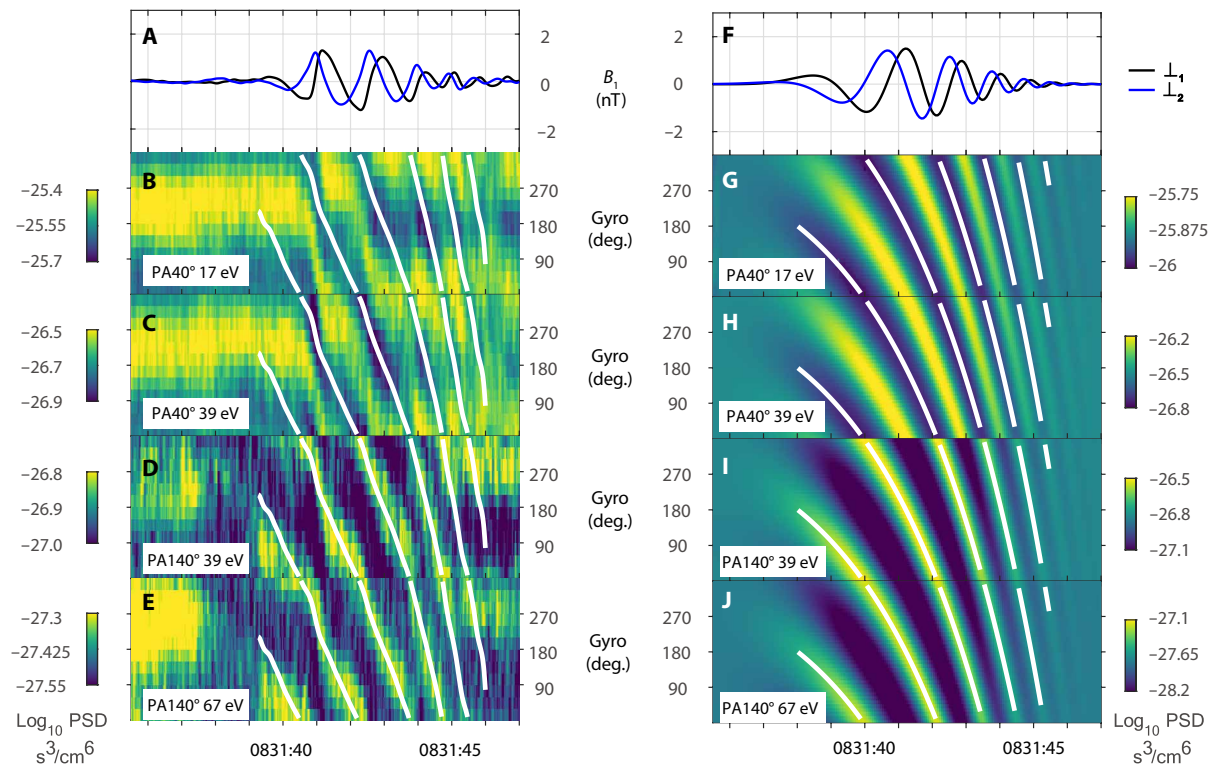
Last, we note that the energized electrons could contribute to the excitation of electron-scale whistler waves at even higher frequencies near 50 Hz (~0.5 $f_{ce}$, where $f_{ce}$ is the electron gyrofrequency). Figure 6 shows the magnetic field and electron measurements during the green-shadowed interval in Fig. 1, in which the variation of the field strength (Fig. 6B) originates from the oblique propagation of the magnetosonic-whistler waves. The field strength minima are clearly associated with peaks in wave power near 50 Hz (Fig. 6C). They are also accompanied by donut-shaped pitch angle distributions (53) for electrons at 25 to 65 eV (Fig. 6D), characterized by reduced and enhanced PSDs at pitch angles near 90° and 60°/120°, respectively. Since these electrons satisfy the cyclotron resonance condition for the whistler waves at ~50 Hz, they could provide the free energy for wave excitation (13, 14). In other words, the 25- to 65-eV electrons could simultaneously resonate with the ion-scale, magnetosonic-whistler waves and the electron-scale, high-frequency whistler waves, which facilitates the cross-scale energy transfer.
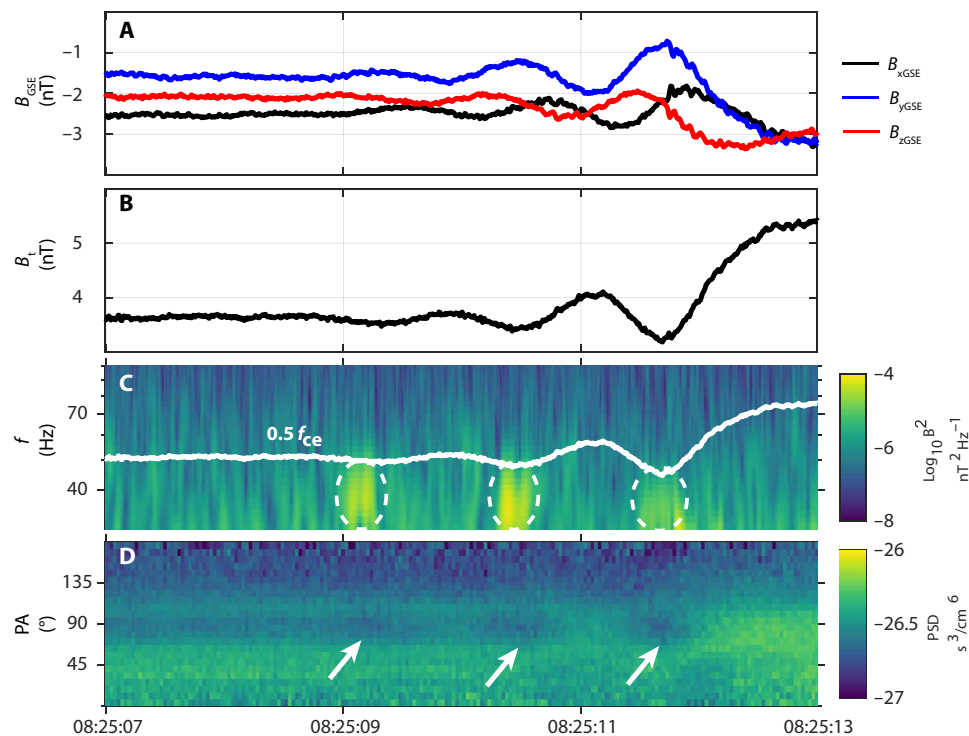
### Event #2
The event discussed above is not unique. Despite the limited availability of the burst-mode, high-resolution MMS data constrained by downlink capacity, we have identified three more events in the foreshock region with similar features of cross-scale wave-particle resonances. One of these events (event #2) is analyzed in this section based on a similar approach, and the other two events are presented



**Fig. 4. Energy transfer and linear instability analysis during the yellow-shadowed interval in Fig. 1.** (**A**) Magnetic field measurements in GSE coordinates. (**B**) Energy transfer rate between the magnetosonic-whistler waves and resonant ions in plasma rest frame. (**C**) Wave growth rate γ (blue line) and dispersion relation ω$_{pl}$ (red line) in the plasma frame. The observed magnetosonic-whistler wave number $k_{pl}$ is around $-k_n$.

**Fig. 5. MMS observations and simulation results of the electron gyro-phase spectra during the yellow-shadowed interval in Fig. 1.** (**A**) Filtered magnetosonic-whistler waves $B_{1,mw}$ in FAC. (**B** and **C**) Gyro-phase spectra for electrons with the pitch angle of 40°, within the 17- and 39-eV energy channels. (**D** and **E**) Gyro-phase spectra for electrons with the pitch angle of 140°, within the 39- and 67-eV energy channels. The phase of $-B_{1,mw}$ is indicated by the white lines. (**F** to **J**) Simulation results in the same format as in (A) to (E).



**Fig. 6. The coupling between the observed magnetosonic-whistler waves (~1 Hz) and high-frequency whistler waves (~50 Hz) from 0825:07 to 0825:13 UT.** (**A**) Magnetic field measurements in GSE coordinates. (**B**) Magnetic field strength. (**C**) Wavelet power spectrum of the magnetic field, with the white line representing the half electron gyrofrequency. (**D**) Pitch angle spectrum of the electron PSDs in the 25- to 65-eV range.

in the Supplementary Materials (as events #S1 and #S2; see figs. S6 and S7).

An overview of event #2 is presented in Fig. 7. Figure 7A shows the magnetic field variations with a period of ~30s, which are also characterized by the in-phase relationship between the field strength and the plasma density (see Fig. 7B). Therefore, they are ULF fast/magnetosonic waves (38, 39). The wavelet power spectrum in Fig. 7C displays the periodic wave power enhancements at frequencies above 0.1 Hz, which, like the case for event #1 (see Fig. 1C), indicates the coupling between the fluid-scale ULF waves and ion-scale magnetosonic-whistler waves. Figure 7D shows the ion pitch angle spectra, in which the solar wind ions with maximum PSDs are concentrated at pitch angles below ~45°. The reflected ions (with pitch angles above ~90°) emerge at ~20:36:10 UT, which is followed by the occurrence of ULF waves at ~20:36:30 UT. This time sequence is also consistent with the scenario of ULF wave excitation by the reflected ions in the foreshock region (17, 42).

After that, the PSDs of the ions within a wide pitch angle range between ~45° and ~135° are enhanced. Figure 7E presents the energy spectrum of the ions moving in the $-z$ direction (with pitch angles around 90°), which displays periodic flux enhancements coinciding with the $B_z$ peaks (the white line). Such an in-phase relationship is confirmed by the enhanced wavelet coherences in Fig. 7F. We next select the red-shadowed interval in Fig. 7A, during which the ULF waves are circularly polarized (see Fig. 7G), to examine the ion gyro-phase spectra at two different pitch angles, ~60° and ~90°. These spectra, shown in Fig. 7 (H to K), display phase-bunched signatures characterized by the periodic occurrence of inclined stripes with enhanced PSDs in antiphase with the wave field $B_{1,ULF}$. Similar to event #1, the phase-bunched signatures are manifestations of anomalous resonance that contributes to the ion acceleration. Note that the ion energy range of the FPI measurements has an upper limit of 30 keV, and therefore, the phase-bunched signatures observed at this energy (see Fig. 7I) implies that the ULF waves may have the potential to accelerate ions at even higher energies. The FEEPS observations displayed in fig. S8 display a remarkable increase in the ion fluxes at a few hundred kilo–electron volts during this time interval, although it is hard to achieve a concrete evidence for anomalous resonance due to the lower resolution of the FEEPS data.

Since the energized ions are separated in phase space from the solar wind population (see Fig. 7D), the unstable ion distributions, like the case in event #1, can naturally excite the ion-scale magnetosonic-whistler waves. We next examine the interaction between the magnetosonic-whistler waves and the electrons. The interaction is made possible by the large wave amplitude, ~5 nT during the yellow-shadowed interval in Fig. 7A. The zoom-in view of this time interval is presented in Fig. 8, with the wave magnetic field (filtered between 0.2 and 2 Hz) given in Fig. 8A. The gyro-phase spectra for 140° pitch angle electrons within a wide energy range (14 to 484 eV), displayed in Fig. 8 (B to F), all exhibit phase-bunched stripes in-phase or in-antiphase with the wave magnetic field. Such an energy dependence of the phase relationship indicates the occurrence of anomalous resonance. The resulting energization can be also visualized in the electron pitch angle spectra (Fig. 8, G and H), with enhanced PSDs near the pitch angle of ~140°. One may also find that the perpendicular-moving electrons are concentrated near the minima of the field strength (the white lines), which indicates the modulation of the electron temperature anisotropy by the ion-scale magnetosonic-whistler waves. It is the temperature anisotropy that drives the

high-frequency whistler waves (~0.5 $f_{ce}$; see Fig. 8I) via cyclotron resonance. Therefore, the observations in event #2 are also consistent with the scenario of cross-scale wave-particle energy transfer.
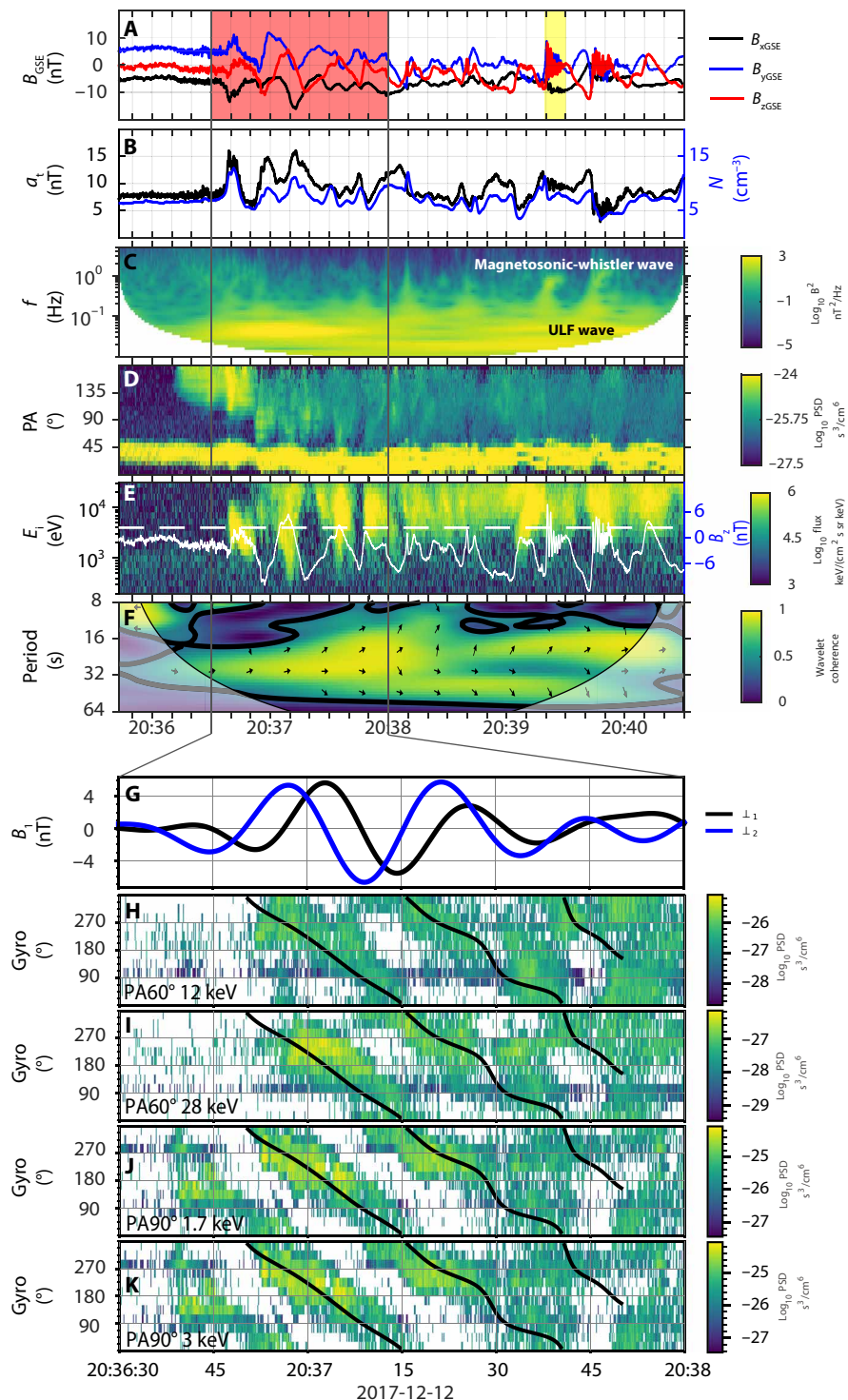
## DISCUSSION

The cartoon in Fig. 9 summarizes the cross-scale energy transfer via multiple coherent wave-particle resonant processes in Earth's foreshock, in which the energy is transferred from fluid to ion scales and eventually to electron scales. More specifically, the magnetosonic waves are excited via cyclotron resonance with the reflected ions backstreaming from the bow shock. As the wave amplitude increases, the resonance condition is nonlinearly revised so that another ion population can be accelerated via anomalous resonance (42). It is this population that leads to the excitation of the magnetosonic-whistler waves, and subsequently, the waves can accelerate the electrons through a simultaneous, anomalous resonance. Moreover, the energized electrons can excite the whistler waves at higher frequencies via cyclotron resonance. In other words, it is the simultaneous and/or successive occurrence of the cyclotron and the anomalous resonances (which correspond to distinct particle species and/or velocities) that accommodates the chain of cross-scale energy transfer. This mechanism could shed light on our understanding of the wave-particle energy transfer in a variety of plasma environments.
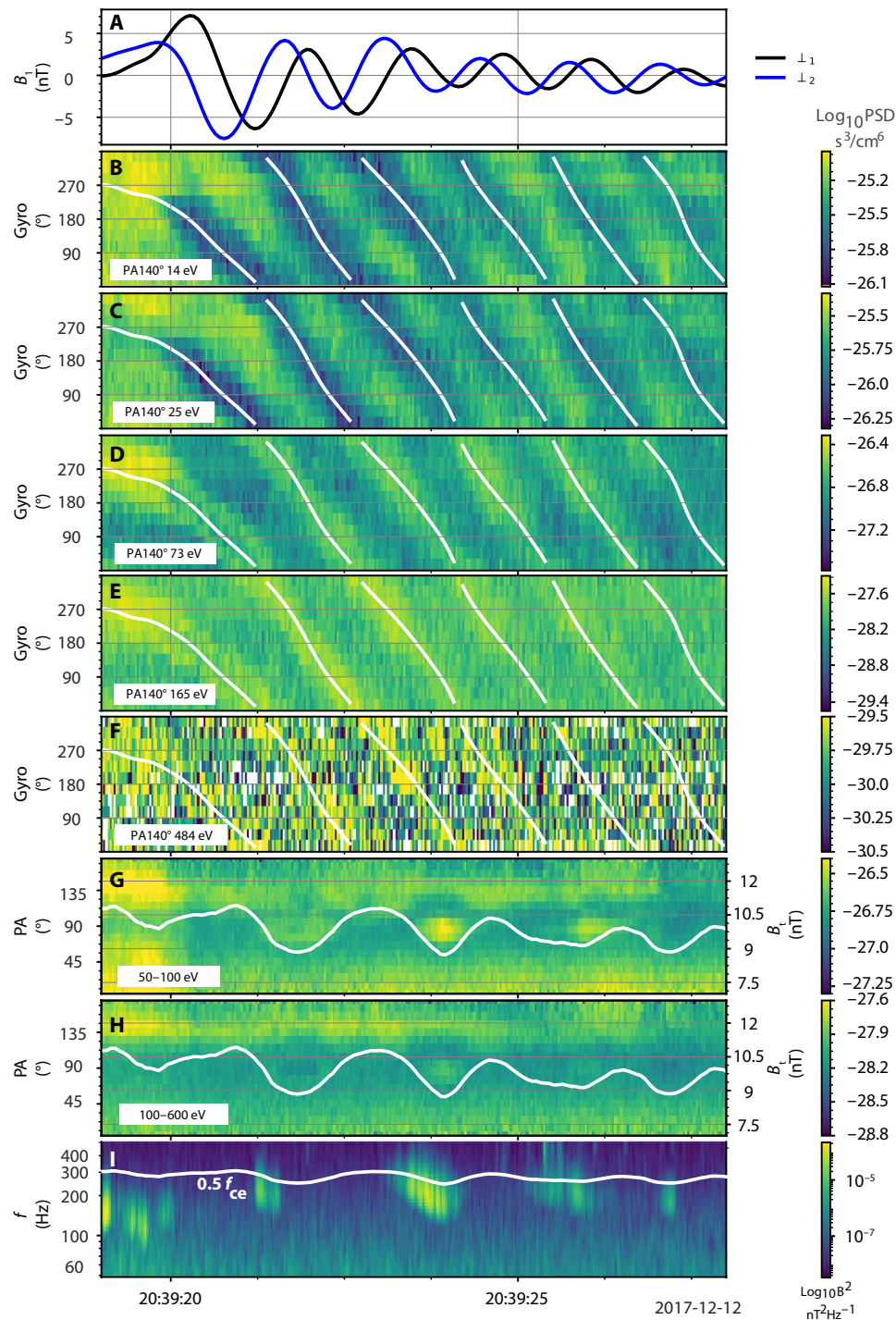
A region of particular interest is the Martian space environment. Recent observations have shown the generation of ULF magnetosonic waves in the Martian foreshock region by resonant interactions with newly ionized atoms in the Martian exosphere (25). The steepening of the ULF waves is also found associated with the high-frequency wave packets (24). The ULF waves may even propagate downstream and resonate with the oxygen ions in the induced magnetosphere [see (57) and Fig. 3E for phase-bunched ion distributions], thereby enhancing the Martian ion escape. These observations are quite consistent with our scenario, except that the newborn ions appear to play the role of the reflected ions in our cases. Since the steepened ULF waves and the associated magnetosonic-whistler waves can also be observed in other planetary or cometary foreshocks (23, 27), we expect that the chain of cross-scale wave-particle energy transfer would also apply to these regions, although it may not be easy to identify observationally the electron-scale processes due to the lack of high-resolution data in regions other than the near-Earth space.

Moreover, we note that collisionless shocks are ubiquitous in the plasma universe playing a key role in the acceleration of charged particles (58, 59). However, the efficient acceleration of the particles requires that they are sufficiently energetic before encountering the shocks, and it remains unclear how these seed particles are produced upstream of the shocks. This is Fermi's so-called injection problem (60, 61). The chain of wave-particle resonances in the foreshock region may be essential for the generation of seed particles. As shown in the analysis of event #2, the ULF waves are associated with enhancements of ion fluxes indicating their acceleration within a wide energy range up to a few hundred kilo–electron volts. For electrons, the critical challenge in the generation of nonthermal electrons from the thermal population (62, 63) could also be tackled. Although the magnetosonic-whistler waves cannot interact with the 0.5-keV electrons through the linear cyclotron resonance (63, 64), the anomalous resonance between them occurs when the wave amplitude becomes large enough. As shown in Fig. 8 (G and H), the nonthermal electron fluxes are enhanced near the pitch angle of
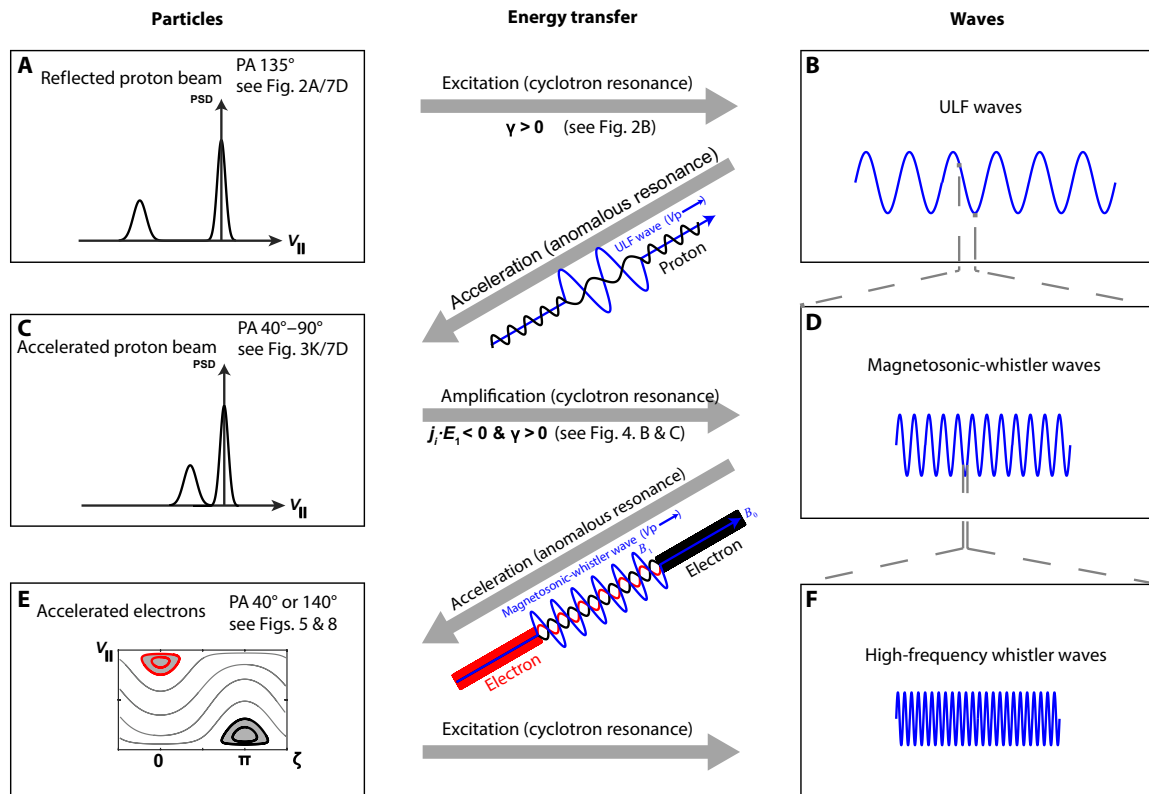
**Fig. 7. MMS observations of the ULF waves and associated ion distributions for event #2.** (**A** to **F**) The same format as in Fig. 1. (**G**) The ULF wave magnetic field $B_{1,ULF}$ in FAC during the red-shadowed interval in (A). (**H** and **I**) Gyro-phase spectra for ions with the pitch angle of 60°, within the 12- and 28-keV energy channels. (**J** and **K**) Gyro-phase spectra for ions with the pitch angle of 90°, within the 1.7- and 3-keV energy channels. The phase of $-\mathbf{B}_{1,ULF}$ is indicated by the black lines.

**Fig. 8. MMS observations of the magnetosonic-whistler waves, the associated electron distributions, and the high-frequency whistler waves during the yellow-shadowed interval in Fig. 7.** (**A**) The magnetosonic-whistler wave magnetic field $\mathbf{B}_{1,mw}$ in FAC. (**B** to **F**) Gyro-phase spectra for electrons with the pitch angle of 140°, within the 14-, 25-, 73-, 165-, and 484-eV energy channels, respectively. The phase of $-\mathbf{B}_{1,mw}$ is indicated by the white lines. (**G** and **H**) Pitch angle spectra for 50- to 100- and 100- to 600-eV electrons, with the white lines representing the magnetic field strength. (**I**) Wavelet power spectrum of magnetic field. The white line represents the half electron gyrofrequency.

**Fig. 9. Schematic illustration of the wave-particle cross-scale energy transfer upstream of the terrestrial bow shock.** (**A**) The shock-reflected ions, with pitch angles of ~135°, provide the initial free energy to linearly excite the ULF waves via cyclotron resonance. (**B**) As the ULF wave amplitude grows, anomalous resonance occurs, and consequently, (**C**) the ions with pitch angles between 40° and 90° are accelerated. (**D**) The accelerated ions contribute to the growth of magnetosonic-whistler waves via cyclotron resonance. (**E**) The large-amplitude magnetosonic-whistler waves accelerate the electrons through anomalous resonance. (**F**) The energized electrons further excite the high-frequency whistler waves. The chain of wave-particle resonances enables an energy transfer from fluid to ion scales and eventually to electron scales.

~140° [at which anomalous resonance occurs; see the phase-bunched features in Fig. 8 (E and F)]. The energized electrons also contribute to the excitation of high-frequency whistler waves (see Figs. 6C and 8I), which in turn could lead to further acceleration of the electrons in the foreshock region (65, 66).

Briefly, we take advantage of the high-resolution MMS observations to explore the cross-scale energy transfer process in the terrestrial foreshock via coherent wave-particle interactions. The process involves multiple plasma waves and particle populations to offer a comprehensive picture of energy transfer and dissipation. Given the ubiquity of shocks in the plasma universe, similar mechanism could apply to a variety of regions including other planetary/cometary space and the interplanetary/interstellar shocks, providing a promising solution to Fermi's injection problem.

## MATERIALS AND METHODS
### Linear instability analysis
The kinetic plasma dispersion relation solver or magnetized and unmagnetized plasma (PDRK) (45) is applied to calculate the wave dispersion relation and the corresponding growth rate in plasma frame. The input parameters derived from observations are as follows.

During the red-shadowed interval in Fig. 1, the background magnetic field is 3 nT. The plasma consists of three components, including the Maxwellian-distributed solar wind ions, electrons, and the shifted-Maxwellian reflected beam (see Fig. 2A). Their temperatures are 10, 10, and 1000 eV, respectively. Their number densities are 4, 4.03, and 0.03 cm$^{-3}$, respectively. The velocity shift for the beam population is 930 km/s. The parameters for the beam population are obtained by integrating the observed ion distributions within the energy range of 2 to 8 keV and the pitch angle range of 90° to 180°.

During the yellow-shadowed interval in Fig. 1, the background magnetic field is also 3 nT. The Maxwellian-distributed solar wind ions and electrons have the same temperature of 10 eV. The number densities are 2 and 2.01 cm$^{-3}$, respectively. The reflected ion population is assumed to be shifted bi-Maxwellian, with a velocity shift of 465 km/s and a number density of 0.01 cm$^{-3}$. The perpendicular and parallel temperatures are 2000 and 1000 eV, respectively. The parameters above are obtained by integrating the observed ion distributions within the pitch angle range of 40° to 90°.

### Simulation setup
The electromagnetic fields in spacecraft frame are expressed, in FAC coordinates, as

$$\mathbf{E} = \mathbf{E_1} = E_{\max}\exp\left[-\frac{(z-v_w t - Z_0)^2}{L^2}\right]\left[\sin\left(k_\parallel z - \omega t\right)\mathbf{x}, -\cos\left(k_\parallel z - \omega t\right)\mathbf{y}\right]$$

$$(4)$$

$$\mathbf{B} = \mathbf{B_0} + \mathbf{B_1} = B_0\mathbf{z} + B_{max}\exp\left[-\frac{(z - v_w t - Z_0)^2}{L^2}\right]$$

$$\left[\cos(k_\| z - \omega t)\mathbf{x}, \sin(k_\| z - \omega t)\mathbf{y}\right] \qquad (5)$$

where ω represents the wave frequency in spacecraft frame. The Gaussian-profiled wave packet propagates at the velocity of $v_w$ along the uniform background magnetic field $B_0$. The Gaussian profile is initially centered at $Z_0$ with a characteristic width $L$. The parallel wave number in spacecraft frame $k_\| = v_w / \omega$ and the wavelength $\lambda = 2\pi / k_\|$ are consequently defined.

For the quasi-monochromatic ULF waves, we assume a constant $\omega_{ULF} = 0.14$ rad s$^{-1}$. Other parameters, determined to match the observations, include $B_0 = 3$ nT, $B_{max} = 2$ nT, $E_{max} = 0.9$ mV m$^{-1}$, $v_{ULF} = 450$ km s$^{-1}$, $k_{ULF} = 3.1 * 10^{-7}$ m$^{-1}$, $\lambda = 2.025 * 10^7$ m, $Z_0 = 5\lambda$, and $L = 2\lambda$.

For the dispersive magnetosonic-whistler waves, the situation is more complicated since the wave phase velocity depends on frequency. In this event, the difference in the wave phase velocity (due to the changing wave frequency) is ~20 km/s, which is much smaller than the typical phase velocity of ~400 km/s. Therefore, we neglect the variations of the wave phase velocity, and the wave packet hardly changes its profile within the time interval of interest. We also assume that the magnetosonic-whistler wave frequency $\omega_{mw}$ decreases exponentially with time

$$\omega_{mw}(z, t) = 0.2\pi\exp\left[(v_{mw}t + Z_1 - z)/L_1\right] \qquad (6)$$

Here, $Z_1$ represents the initial position where the wave frequency is $0.2\pi$, and $L_1$ represents the characteristic width of the frequency profile. With a fixed wave phase speed $v_{mw}$, the parallel wave number $k_{mw}(z, t) = \omega_{mw}(z, t) / v_{mw}$ and the wavelength $\lambda_{mw}(z, t)$ are consequently determined as functions of position and time, in spacecraft frame. The parameters for the whistler waves are $B_0 = 2$ nT, $B_{max} = 1.5$ nT, $E_{max} = 0.6$ mV m$^{-1}$, $v_{mw} = 400$ km s$^{-1}$, $Z_0 = -3.5 * 10^6$ m, $L = 10^6$ m, $Z_1 = -2.4 * 10^6$ m, and $L_1 = 2 * 10^6$ m.

In the simulation, the initial ion distributions are obtained by direct observations (the averaged measurements between 0816:00 and 0817:00). The initial electron distributions are assumed to be shifted bi-Maxwellian, expressed as

$$f = n_0\left(\frac{m}{2\pi T_\perp}\right)\left(\frac{m}{2\pi T_\|}\right)^{\frac{1}{2}}\exp\left[-\frac{mV_x^2 + mV_y^2}{2T_\perp} - \frac{m(V_z - V_e)^2}{2T_\|}\right] \qquad (7)$$

where the parameters include the parallel bulk velocity $V_e = 450$ km s$^{-1}$, parallel temperature $T_\| = 20$ eV, perpendicular temperature $T_\perp = 10$ eV, and electron number density $n_0 = 1.8$ cm$^{-3}$. These parameters are determined from the MMS FPI measurements.

The immobile virtual spacecraft is located at (0,0,0) in this simulation, which obtains the proton velocity distributions every 3 s. At any given time, 12 protons (evenly distributed in the perpendicular plane, with 30° gyro-phase interval) with the same kinetic energy and pitch angle are traced backward to obtain their initial positions in the velocity phase space. The phase space density for each bin is consequently determined by tracing its corresponding particle via the Liouville's theorem. For the electrons, the time resolution is 0.06 s, and the gyro-phase interval is 10°.

## Wave-particle resonance conditions

In our analysis of wave-particle interactions, the cyclotron resonance (including the normal and the anomalous cyclotron resonances) and the anomalous resonance are invoked. To avoid confusion, we present below the derivation of these resonance conditions from the equations of particle motion. For simplicity, we focus on the proton behavior in the parallel-propagating, left-hand polarized waves, and the other situations can be derived similarly.

We first follow (*34*) to describe the particle velocity vector **v** by its parallel velocity $v_\|$, perpendicular velocity $v_\perp$, and gyro-phase angle $\phi_v$, defined in FAC coordinates. There are three forces in the perpendicular plane, including $q\mathbf{v_\perp} \times \mathbf{B_0}$, $q\mathbf{v_\|} \times \mathbf{B_1}$, and $q\mathbf{E_1}$, with the latter two associated with the wave field. The proton angular velocity is consequently expressed as

$$\frac{d\phi_v}{dt} = -\frac{qB_0}{m} - \frac{q}{m}\left(E_1 - v_\| B_1\right)\frac{\cos\zeta}{v_\perp} = -\Omega + \Omega_1\left(v_\| - v_w\right)\frac{\cos\zeta}{v_\perp} \qquad (8)$$

where $\zeta = \phi_v - \phi_B$ is the phase difference between the particle perpendicular velocity $\mathbf{v_\perp}$ and the wave field $\mathbf{B_1}$, $v_w$ is the wave propagation speed, $\Omega = B_0 q / m$ is the gyrofrequency, and $\Omega_1 = B_1 q / m$ is the nominal gyrofrequency associated with the wave field $B_1$. The second right-hand side term in Eq. 8 originates from the two wave-associated forces. When they are negligible (a most typical assumption), the particle's angular velocity is simply the gyrofrequency $\Omega$, and the time derivative of $\zeta$ is given by

$$\frac{d\zeta}{dt} = \frac{d\phi_v}{dt} - \frac{d\phi_B}{dt} = \omega - k_\| v_\| - \Omega \qquad (9)$$

For those protons with a parallel velocity

$$V_r = \frac{\omega - \Omega}{k_\|} \qquad (10)$$

Eq. 9 equals zero to indicate the occurrence of the normal cyclotron resonance. In this case, the wave frequency observed by the resonant particle, after considering the Doppler shift to the particle's guiding center frame, matches its gyrofrequency. Therefore, the particle could stay in a constant wave phase to enable a sustained energy transfer, although in the nonlinear regime, the particle's energy variation would also indicate a gradual deviation of $v_\|$ from the resonance velocity (10). According to the nonlinear cyclotron resonance theory (*43*, *44*), the ζ variations for resonant particles are periodic, to form closed trajectories in the $v_\|$-ζ phase space.

For right-hand polarized waves, the reversed time derivative of $\phi_B$ indicates that Eq. 9 should be replaced by

$$\frac{d\zeta}{dt} = k_\| v_\| - \omega - \Omega \qquad (11)$$

By having Eq. 11 equal to zero, we obtain the anomalous cyclotron resonance velocity

$$V_r = \frac{\omega + \Omega}{k_\|} \qquad (12)$$

which occurs as the particle's guiding center overtakes the waves so that the wave polarization seen by the particle could be reversed by the Doppler effect. Obviously, the same nonlinear effect discussed before also applies in this case.

The above derivations for normal and anomalous cyclotron resonances neglect the second right-hand side term in Eq. 8. However,

this term can become comparable to the first right-hand side term in Eq. 8 if criterion (3) is unsatisfied. By keeping this term in Eq. 8, the time derivative of $\zeta$ can be expressed by

$$\frac{d\zeta}{dt} = k_\parallel v_\parallel - \omega - \Omega + \Omega_1 \left( v_\parallel - v_w \right) \frac{\cos\zeta}{v_\perp} \qquad (13)$$

By having Eq. 13 equal to zero, we obtain the resonance velocity given in Eq. 2. The resonance is termed anomalous resonance, which occurs when the wave field is strong enough to modify the particle's angular velocity from $\Omega$. More detailed discussions on anomalous resonance are given in (34).

## Supplementary Materials

**This PDF file includes:**
Supplementary Text
Figs. S1 to S8
Tables S1 and S2

## REFERENCES AND NOTES

1. P. Grete, B. W. O'Shea, K. Beckwith, W. Schmidt, A. Christlieb, Energy transfer in compressible magnetohydrodynamic turbulence. *Phys. Plasmas* **24**, 092311 (2017).

2. P. L. Johnson, Energy transfer from large to small scales in turbulence by multiscale nonlinear strain and vorticity interactions. *Phys. Rev. Lett.* **124**, 104501 (2020).

3. J.-H. Li, F. Yang, X.-Z. Zhou, Q.-G. Zong, A. V. Artemyev, R. Rankin, Q. Shi, S. Yao, H. Liu, J. He, Z. Fu, C. Xiao, J. Liu, C. Pollock, G. Le, J. L. Burch, Self-consistent kinetic model of nested electron- and ion-scale magnetic cavities in space plasmas. *Nat. Commun.* **11**, 5616 (2020).

4. D. Manzini, F. Sahraoui, F. Califano, Subion-scale turbulence driven by magnetic reconnection. *Phys Rev Lett* **130**, 205201 (2023).

5. C. A. Towery, A. Y. Poludnenko, J. Urzay, J. O'Brien, M. Ihme, P. E. Hamlington, Spectral kinetic energy transfer in turbulent premixed reacting flows. *Phys Rev E* **93**, 053115 (2016).

6. I. Y. Vasko, O. V. Agapitov, F. S. Mozer, J. W. Bonnell, A. V. Artemyev, V. V. Krasnoselskikh, Y. Tong, Electrostatic steepening of whistler waves. *Phys. Rev. Lett.* **120**, 195101 (2018).

7. I. Y. Vasko, F. S. Mozer, T. Bowen, J. Verniero, X. An, A. Artemyev, S. D. Bale, J. W. Bonnell, J. Halekas, I. V. Kuzichev, Resonance of low-frequency electromagnetic and ion-sound modes in the solar wind. *Astrophys. J. Lett.* **967**, L31 (2024).

8. X. An, J. Bortnik, X. J. Zhang, Nonlinear Landau resonant interaction between kinetic Alfvén waves and thermal electrons: Excitation of time domain structures. *J. Geophys. Res.* **126**, e2020JA028643 (2021).

9. K. Asamura, M. Shoji, Y. Miyoshi, Y. Kasahara, Y. Kasaba, A. Kumamoto, F. Tsuchiya, S. Matsuda, A. Matsuoka, M. Teramoto, Y. Kazama, I. Shinohara, Cross-energy couplings from magnetosonic waves to electromagnetic ion cyclotron waves through cold ion heating inside the plasmasphere. *Phys. Rev. Lett.* **127**, 245101 (2021).

10. L. Li, Y. Omura, X. Z. Zhou, Q. G. Zong, R. Rankin, C. Yue, S. Y. Fu, J. Ren, Chorus wave generation modulated by field line resonance and mirror-mode ULF waves. *J. Geophys. Res.* **128**, e2022JA031127 (2023).

11. Z. Xia, L. Chen, L. Dai, S. G. Claudepierre, A. A. Chan, A. R. Soto-Chavez, G. D. Reeves, Modulation of chorus intensity by ULF waves deep in the inner magnetosphere. *Geophys. Res. Lett.* **43**, 9444–9452 (2016).

12. X. J. Zhang, L. Chen, A. V. Artemyev, V. Angelopoulos, X. Liu, Periodic excitation of chorus and ECH waves modulated by ultralow frequency compressions. *J. Geophys. Res.* **124**, 8535–8550 (2019).

13. R. Chen, X. Gao, Z. Yang, Q. Lu, Z. Kong, J. Ma, Y. Ke, C. Wang, Cross-scale energy transfer from ion-scale to electron-scale waves in the Earth's foreshock region. *J. Geophys. Res.* **129**, e2024JA032567 (2024).

14. S. T. Yao, Q. Q. Shi, Q. G. Zong, A. W. Degeling, R. L. Guo, L. Li, J. X. Li, A. M. Tian, H. Zhang, Z. H. Yao, H. S. Fu, C. M. Liu, W. J. Sun, Z. Niu, W. Y. Li, Z. Y. Liu, O. Le Contel, S. Zhang, C. Xiao, W. S. Shang, R. B. Torbert, R. E. Ergun, P. A. Lindqvist, C. J. Pollock, Low-frequency whistler waves modulate electrons and generate higher-frequency whistler waves in the solar wind. *Astrophys. J.* **923**, 216 (2021).

15. L. B. Wilson III, Low frequency waves at and upstream of collisionless shocks in *Low-frequency Waves in Space Plasmas* [American Geophysical Union (AGU), 2016], chap. 16, pp. 269–291.

16. H. Zhang, Q. Zong, H. Connor, P. Delamere, G. Facskó, D. Han, H. Hasegawa, E. Kallio, Á. Kis, G. Le, B. Lembège, Y. Lin, T. Liu, K. Oksavik, N. Omidi, A. Otto, J. Ren, Q. Shi, D. Sibeck, S. Yao, Dayside transient phenomena and their impact on the magnetosphere and ionosphere. *Space Sci. Rev.* **218**, 40 (2022).

17. S. P. Gary, Electromagnetic ion/ion instabilities and their consequences in space plasmas: A review. *Space Sci. Rev.* **56**, 373–415 (1991).

18. G. Le, C. T. Russell, E. J. Smith, Discrete wave packets upstream from the Earth and comets. *J. Geophys. Res.* **94**, 3755–3760 (1989).

19. N. Omidi, D. Winske, Steepening of kinetic magnetosonic waves into shocklets: Simulations and consequences for planetary shocks and comets. *J. Geophys. Res.* **95**, 2281–2300 (1990).

20. M. Hoppe, C. Russell, Whistler mode wave packets in the Earth's foreshock region. *Nature* **287**, 417–420 (1980).

21. M. Hoppe, C. Russell, On the nature of ULF waves upstream of planetary bow shocks. *Adv. Space Res.* **1**, 327–332 (1981).

22. L. B. Wilson, C. A. Cattell, P. J. Kellogg, K. Goetz, K. Kersten, J. C. Kasper, A. Szabo, K. Meziane, Low-frequency whistler waves and shocklets observed at quasi-perpendicular interplanetary shocks. *J. Geophys. Res.* **114**, A10106 (2009).

23. C. Bertucci, N. Achilleos, C. Mazelle, G. B. Hospodarsky, M. Thomsen, M. K. Dougherty, W. Kurth, Low-frequency waves in the foreshock of Saturn: First results from Cassini. *J. Geophys. Res.* **112**, A09219 (2007).

24. L. Shan, A. Du, B. T. Tsurutani, Y. S. Ge, Q. Lu, C. Mazelle, C. Huang, K.-H. Glassmeier, P. Henri, In situ observations of the formation of periodic collisionless plasma shocks from fast mode waves. *Astrophys. J.* **888**, L17 (2020).

25. L. Shan, B. T. Tsurutani, Y. Ohsawa, C. Mazelle, C. Huang, A. Du, Y. S. Ge, Q. Lu, Observational evidence for fast mode periodic small-scale shocks: A new type of plasma phenomenon. *Astrophys. J. Lett.* **905**, L4 (2020).

26. B. T. Tsurutani, D. J. Southwood, E. J. Smith, A. Balogh, A survey of low frequency waves at Jupiter: The Ulysses encounter. *J. Geophys. Res.* **98**, 21203–21216 (1993).

27. K. Ostaszewski, K.-H. Glassmeier, C. Goetz, P. Heinisch, P. Henri, S. A. Park, H. Ranocha, I. Richter, M. Rubin, B. Tsurutani, Steepening of magnetosonic waves in the inner coma of comet 67P/Churyumov–Gerasimenko. *Ann. Geophys.* **39**, 721–742 (2021).

28. B. T. Tsurutani, E. J. Smith, Hydromagnetic waves and instabilities associated with cometary ion pickup: ICE observations. *Geophys. Res. Lett.* **13**, 263–266 (1986).

29. J.-H. Li, X.-Z. Zhou, Z.-Y. Liu, S. Wang, A. V. Artemyev, Y. Omura, X.-J. Zhang, L. Li, C. Yue, Q.-G. Zong, C. Pollock, G. Le, J. L. Burch, Identification of coupled Landau and anomalous resonances in space plasmas. *Phys. Rev. Lett.* **133**, 035201 (2024).

30. Z. Y. Liu, B. Wang, Q. G. Zong, S. T. Yao, C. J. Pollock, G. Le, Thermal electron behavior in obliquely propagating whistler waves: MMS observations in the solar wind. *Geophys. Res. Lett.* **48**, e2021GL094099 (2021).

31. Z. Y. Liu, Q. G. Zong, H. Zhang, J. T. Zhao, R. Rankin, C. J. Pollock, G. Le, Ion behavior at shocklets: A case study of MMS observations. *Geophys. Res. Lett.* **49**, e00449 (2022).

32. S. Wang, L. J. Chen, J. Ng, N. Bessho, G. Le, S. F. Fung, D. J. Gershman, B. L. Giles, A case study of nonresonant mode 3-s ULF waves observed by MMS. *J. Geophys. Res.* **125**, e2020JA028557 (2020).

33. S. Wang, J. H. Li, L. Li, X. Z. Zhou, Y. Omura, J. T. Zhao, Z. Y. Liu, Q. G. Zong, H. Zhang, C. Yue, A statistical examination of interactions between 1-Hz whistler waves and ions in the Earth's foreshock. *J. Geophys. Res.* **129**, e2024JA032960 (2024).

34. J.-H. Li, Z.-Y. Liu, X.-Z. Zhou, L. Li, Y. Omura, C. Yue, Q.-G. Zong, Z.-Y. Pu, S.-Y. Fu, L. Xie, C. T. Russell, C. J. Pollock, G. Le, J. L. Burch, Anomalous resonance between low-energy particles and electromagnetic plasma waves. *Commun. Phys.* **5**, 300 (2022).

35. R. B. Torbert, C. T. Russell, W. Magnes, R. E. Ergun, P.-A. Lindqvist, O. Lecontel, H. Vaith, J. Macri, S. Myers, D. Rau, J. Needell, B. King, M. Granoff, M. Chutter, I. Dors, G. Olsson, Y. V. Khotyaintsev, A. Eriksson, C. A. Kletzing, S. Bounds, B. Anderson, W. Baumjohann, M. Steller, K. Bromund, G. Le, R. Nakamura, R. J. Strangeway, H. K. Leinweber, S. Tucker, J. Westfall, D. Fischer, F. Plaschke, J. Porter, K. Lappalainen, The FIELDS instrument suite on MMS: Scientific objectives, measurements, and data products. *Space Sci. Rev.* **199**, 105–135 (2016).

36. C. Pollock, T. Moore, A. Jacques, J. Burch, U. Gliese, Y. Saito, T. Omoto, L. Avanov, A. Barrie, V. Coffey, J. Dorelli, D. Gershman, B. Giles, T. Rosnack, C. Salo, S. Yokota, M. Adrian, C. Aoustin, C. Auletti, S. Aung, V. Bigio, N. Cao, M. Chandler, D. Chornay, K. Christian, G. Clark, G. Collinson, T. Corris, A. D. L. Santos, R. Devlin, T. Diaz, T. Dickerson, C. Dickson, A. Diekmann, F. Diggs, C. Duncan, A. Figueroa-Vinas, C. Firman, M. Freeman, N. Galassi, K. Garcia, G. Goodhart, D. Guerrero, J. Hageman, J. Hanley, E. Hemminger, M. Holland, M. Hutchins, T. James, W. Jones, S. Kreisler, J. Kujawski, V. Lavu, J. Lobell, E. LeCompte, A. Lukemire, E. MacDonald, A. Mariano, T. Mukai, K. Narayanan, Q. Nguyan, M. Onizuka, W. Paterson, S. Persyn, B. Piepgrass, F. Cheney, A. Rager, T. Raghuram, A. Ramil, L. Reichenthal, H. Rodriguez, J. Rouzaud, A. Rucker, Y. Saito, M. Samara, J. A. Sauvaud, D. Schuster, M. Shappirio, K. Shelton, D. Sher, D. Smith, K. Smith, S. Smith, D. Steinfeld, R. Szymkiewicz, K. Tanimoto, J. Taylor, C. Tucker, K. Tull, A. Uhl, J. Vloet, P. Walpole, S. Weidner, D. White, G. Winkert, P. S. Yeh, M. Zeuch, Fast plasma investigation for magnetospheric multiscale. *Space Sci. Rev.* **199**, 331–406 (2016).

37. J. B. Blake, B. H. Mauk, D. N. Baker, P. Carranza, J. H. Clemmons, J. Craft, W. R. Crain, A. Crew, Y. Dotan, J. F. Fennell, R. H. Friedel, L. M. Friesen, F. Fuentes, R. Galvan, C. Ibscher, A. Jaynes, N. Katz, M. Lalic, A. Y. Lin, D. M. Mabry, T. Nguyen, C. Pancratz, M. Redding, G. D. Reeves, S. Smith, H. E. Spence, J. Westlake, The fly's eye energetic particle spectrometer (FEEPS)

sensors for the magnetospheric multiscale (MMS) mission. *Space Sci. Rev.* **199**, 309–329 (2016).

38. J. P. Eastwood, A. Balogh, M. W. Dunlop, T. S. Horbury, I. Dandouras, Cluster observations of fast magnetosonic waves in the terrestrial foreshock. *Geophys. Res. Lett.* **29**, 3-1-3-4 (2002).

39. M. M. Hoppe, C. T. Russell, Plasma rest frame frequencies and polarizations of the low-frequency upstream waves: ISEE 1 and 2 Observations. *J. Geophys. Res.* **88**, 2021–2027 (1983).

40. D. A. Tidman, T. G. Northrop, Emission of plasma waves by the Earth's bow shock. *J. Geophys. Res.* **73**, 1543–1553 (1968).

41. O. Santolík, M. Parrot, F. Lefeuvre, Singular value decomposition methods for wave propagation analysis. *Radio Sci.* **38**, 1010 (2003).

42. C. Mazelle, K. Meziane, D. LeQuéau, M. Wilber, J. P. Eastwood, H. Rème, J. A. Sauvaud, J. M. Bosqued, I. Dandouras, M. McCarthy, L. M. Kistler, B. Klecker, A. Korth, M. B. Bavassano-Cattaneo, G. Pallocchia, R. Lundin, A. Balogh, Production of gyrating ions from nonlinear wave–particle interaction upstream from the Earth's bow shock: A case study from Cluster-CIS. *Planet. Space Sci.* **51**, 785–795 (2003).

43. L. Li, Y. Omura, X. Z. Zhou, Q. G. Zong, R. Rankin, C. Yue, S. Y. Fu, Nonlinear wave growth analysis of chorus emissions modulated by ULF waves. *Geophys. Res. Lett.* **49**, e2022GL097978 (2022).

44. Y. Omura, Nonlinear wave growth theory of whistler-mode chorus and hiss emissions in the magnetosphere. *Earth Planets Space* **73**, 95 (2021).

45. H. Xie, Y. Xiao, PDRK: A general kinetic dispersion relation solver for magnetized plasma. *Plasma Sci. Technol.* **18**, 97–107 (2016).

46. B. T. Tsurutani, R. M. Thorne, E. J. Smith, J. T. Gosling, H. Matsumoto, Steepened magnetosonic waves at comet Giacobini-Zinner. *J. Geophys. Res.* **92**, 11074–11082 (1987).

47. A. Grinsted, J. C. Moore, S. Jevrejeva, Application of the cross wavelet transform and wavelet coherence to geophysical time series. *Nonlinear Process. Geophys.* **11**, 561–566 (2004).

48. N. Kitamura, M. Kitahara, M. Shoji, Y. Miyoshi, H. Hasegawa, S. Nakamura, Y. Katoh, Y. Saito, S. Yokota, D. J. Gershman, A. F. Vinas, B. L. Giles, T. E. Moore, W. R. Paterson, C. J. Pollock, C. T. Russell, R. J. Strangeway, S. A. Fuselier, J. L. Burch, Direct measurements of two-way wave-particle energy transfer in a collisionless space plasma. *Science* **361**, 1000–1003 (2018).

49. Z. Y. Liu, Q. G. Zong, R. Rankin, H. Zhang, Y. F. Wang, X. Z. Zhou, S. Y. Fu, C. Yue, X. Y. Zhu, C. J. Pollock, S. A. Fuselier, G. Le, Simultaneous macroscale and microscale wave-ion interaction in near-earth space plasmas. *Nat. Commun.* **13**, 5593 (2022).

50. M. Kitahara, Y. Katoh, Anomalous trapping of low pitch angle electrons by coherent whistler mode waves. *J. Geophys. Res.* **124**, 5568–5583 (2019).

51. J. M. Albert, A. V. Artemyev, W. Li, L. Gan, Q. Ma, Models of resonant wave-particle interactions. *J. Geophys. Res.* **126**, e2021JA029216 (2021).

52. A. Artemyev, A. Neishtadt, J. Albert, L. Gan, W. Li, Q. Ma, Theoretical model of the nonlinear resonant interaction of whistler-mode waves and field-aligned electrons. *Phys. Plasmas* **28**, 052902 (2021).

53. J. H. Li, X. Z. Zhou, Q. G. Zong, F. Yang, S. Fu, S. Yao, J. Liu, Q. Shi, On the origin of donut-shaped electron distributions within magnetic cavities. *Geophys. Res. Lett.* **48**, e2020GL091613 (2021).

54. S. J. Schwartz, P. W. Daly, A. N. Fazakerley, Multi-spacecraft analysis of plasma kinetics. *ISSI Sci. Rep. Ser.* **1,** 159–184 (1998).

55. X. Z. Zhou, A. Runov, V. Angelopoulos, A. V. Artemyev, J. Birn, On the acceleration and anisotropy of ions within magnetotail dipolarizing flux bundles. *J. Geophys. Res.* **123**, 429–442 (2018).

56. N. Kitamura, M. Shoji, S. Nakamura, M. Kitahara, T. Amano, Y. Omura, H. Hasegawa, S. A. Boardsen, Y. Miyoshi, Y. Katoh, M. Teramoto, Y. Saito, S. Yokota, M. Hirahara, D. J. Gershman, B. L. Giles, C. T. Russell, R. J. Strangeway, N. Ahmadi, P. A. Lindqvist, R. E. Ergun, S. A. Fuselier, J. L. Burch, Energy transfer between hot protons and electromagnetic ion cyclotron waves in compressional Pc5 ultra-low frequency waves. *J. Geophys. Res.* **126**, e2020JA028912 (2021).

57. J.-T. Zhao, Q.-G. Zong, Z.-Y. Liu, X.-Z. Zhou, S. Wang, W.-H. Ip, C. Yue, J.-H. Li, Y.-X. Hao, R. Rankin, A. Degeling, S. -Y. Fu, H. Zou, Y. -F. Wang, On energization and loss of the ionized heavy atom and molecule in Mars' atmosphere. arXiv:2410.00832 [physics. space-ph] (2024).

58. E. Lichko, J. Egedal, Magnetic pumping model for energizing superthermal particles applied to observations of the Earth's bow shock. *Nat. Commun.* **11**, 2942 (2020).

59. A. Masters, L. Stawarz, M. Fujimoto, S. J. Schwartz, N. Sergis, M. F. Thomsen, A. Retinò, H. Hasegawa, B. Zieger, G. R. Lewis, A. J. Coates, P. Canu, M. K. Dougherty, Electron acceleration to relativistic energies at a strong quasi-parallel shock wave. *Nat. Phys.* **9**, 164–167 (2013).

60. A. Kis, O. Agapitov, V. Krasnoselskikh, Y. V. Khotyaintsev, I. Dandouras, I. Lemperger, V. Wesztergom, Gyrosurfing acceleration of ions in front of Earth's quasi-parallel bow shock. *Astrophys. J.* **771**, 4 (2013).

61. D. L. Turner, L. B. Wilson III, T. Z. Liu, I. J. Cohen, S. J. Schwartz, A. Osmane, J. F. Fennell, J. H. Clemmons, J. B. Blake, J. Westlake, B. H. Mauk, A. N. Jaynes, T. Leonard, D. N. Baker, R. J. Strangeway, C. T. Russell, D. J. Gershman, L. Avanov, B. L. Giles, R. B. Torbert, J. Broll, R. G. Gomez, S. A. Fuselier, J. L. Burch, Autogenous and efficient acceleration of energetic ions upstream of Earth's bow shock. *Nature* **561**, 206–210 (2018).

62. M. Oka, L. B. W. Iii, T. D. Phan, A. J. Hull, T. Amano, M. Hoshino, M. R. Argall, O. L. Contel, O. Agapitov, D. J. Gershman, Y. V. Khotyaintsev, J. L. Burch, R. B. Torbert, C. Pollock, J. C. Dorelli, B. L. Giles, T. E. Moore, Y. Saito, L. A. Avanov, W. Paterson, R. E. Ergun, R. J. Strangeway, C. T. Russell, P. A. Lindqvist, Electron scattering by high-frequency whistler waves at Earth's bow shock. *Astrophys. J. Lett.* **842**, L11 (2017).

63. M. Oka, F. Otsuka, S. Matsukiyo, L. B. Wilson, M. R. Argall, T. Amano, T. D. Phan, M. Hoshino, O. L. Contel, D. J. Gershman, J. L. Burch, R. B. Torbert, J. C. Dorelli, B. L. Giles, R. E. Ergun, C. T. Russell, P. A. Lindqvist, Electron scattering by low-frequency whistler waves at Earth's bow shock. *Astrophys. J.* **886**, 53 (2019).

64. L. B. Wilson III, D. G. Sibeck, A. W. Breneman, O. L. Contel, C. Cully, D. L. Turner, V. Angelopoulos, D. M. Malaspina, Quantified energy dissipation rates in the terrestrial bow shock: 2. Waves and dissipation. *J. Geophys. Res.* **119**, 6475–6495 (2014).

65. T. Amano, T. Katou, N. Kitamura, M. Oka, Y. Matsumoto, M. Hoshino, Y. Saito, S. Yokota, B. L. Giles, W. R. Paterson, C. T. Russell, O. Le Contel, R. E. Ergun, P. A. Lindqvist, D. L. Turner, J. F. Fennell, J. B. Blake, Observational evidence for stochastic shock drift acceleration of electrons at the Earth's bow shock. *Phys. Rev. Lett.* **124**, 065101 (2020).

66. A. V. Artemyev, X. Shi, T. Z. Liu, X. J. Zhang, I. Vasko, V. Angelopoulos, Electron resonant interaction with whistler waves around foreshock transients and the bow shock behind the terminator. *Journal of Geophysical Research: Space Physics* **127**, e2021JA029820 (2022).

67. J. Li, X. Zhou, Direct observations of cross-scale wave-particle energy transfer in space plasmas. Zenodo 10.5281/zenodo.13947440 (2024); https://doi.org/10.5281/zenodo.13947440.